

Cite this: *Chem. Sci.*, 2019, **10**, 8323 All publication charges for this article have been paid for by the Royal Society of Chemistry

## A symbiotic hetero-nanocomposite that stabilizes unprecedented $\text{CaCl}_2$ -type $\text{TiO}_2$ for enhanced solar-driven hydrogen evolution reaction†

Yuelan Zhang,  <sup>a</sup> Liping Li,  <sup>a</sup> Yan Liu, <sup>a</sup> Tao Feng, <sup>a</sup> Shibo Xi, <sup>b</sup> Xiyang Wang, <sup>a</sup> Chenglin Xue, <sup>a</sup> Jingyu Qian<sup>c</sup> and Guangshe Li  <sup>a</sup>

Symbiotic hetero-nanocomposites prevail in many classes of minerals, functional substances and/or devices. However, design and development of a symbiotic hetero-nanocomposite that contains unachievable phases remain a significant challenge owing to the tedious formation conditions and the need for precise control over atomic nucleation in synthetic chemistry. Herein, we report a solution chemistry approach for a symbiotic hetero-nanocomposite that contains an unprecedented  $\text{CaCl}_2$ -type titania phase inter-grown with rutile  $\text{TiO}_2$ .  $\text{CaCl}_2$  structured  $\text{TiO}_2$ , usually occurring when bulk rutile- $\text{TiO}_2$  is compressed at an extreme pressure of several GPa, is identified to be a distorted structure with a tilt of adjacent ribbons of the *c*-axis of rutile. The structural specificity of the symbiotic  $\text{CaCl}_2$ /rutile  $\text{TiO}_2$  hetero-nanocomposite was confirmed by Rietveld refinement, HRTEM, EXAFS, and Raman spectra, and the formation region ( $\text{TiCl}_4$  concentration vs. reaction temperature) was obtained by mapping the phase diagram. Due to the symbiotic relationship, this  $\text{CaCl}_2$ -type  $\text{TiO}_2$  maintained a high stability *via* tight connection by edge dislocations with rutile  $\text{TiO}_2$ , thus forming a  $\text{CaCl}_2$ /rutile  $\text{TiO}_2$  heterojunction with a higher reduction capacity and enhanced charge separation efficiency. These merits endow symbiotic  $\text{CaCl}_2$ /rutile  $\text{TiO}_2$  with a water splitting activity far superior to that of the commercial benchmark photocatalyst, P25 under simulated sunlight without the assistance of a cocatalyst. Our findings reported here may offer several useful understandings of the mechanical intergrowth process in functional symbiotic hetero-nanocomposites for super interfacial charge separation, where interfacial dislocation appears to be a universal cause.

Received 12th March 2019  
Accepted 22nd July 2019DOI: 10.1039/c9sc01216h  
[rsc.li/chemical-science](http://rsc.li/chemical-science)

## Introduction

Symbiotic hetero-nanocomposites prevail in many classes of minerals, functional substances and/or devices,<sup>1–3</sup> providing opportunities to maximize interfacial/surface chemical reactions and synergistic effects between components essential for important applications. Important applications of these hetero-nanocomposites have been witnessed in a variety of fields, including catalysis, photovoltaic conversion, energy storage, decontamination, and clean energy production since these nanocomposites are merited by optimum interfacial/surface chemical reactions and synergistic effects of components.<sup>4–8</sup> Depending on the interconnection of each component through

van der Waals forces or covalent bonds and on the interplay of individual components, heterogeneous composites could always generate a superior performance. For example, strong interfacial interactions in between components enable charge transfer within heterogeneous composites, accounting for the effective separation of photo-generated electrons and holes through interfaces for excellent photocatalytic overall water splitting activities.<sup>9–14</sup> When noble metals are strongly supported onto oxides in forming heterogeneous composites, excellent CO oxidation ability was achieved because of the simultaneous CO adsorption of noble metals and oxygen activation of  $\text{MO}_x$ .<sup>15–17</sup> Indeed, when growing nanocomposites or epitaxial oxide films, pronounced interfacial interactions could be possible because of the interfacial dislocations that directly influence the average stress and strain states in the composites,<sup>18</sup> while upon cooling down from the growth temperature, tensile strain is stored in the composites or films (owing to the thermal expansion mismatch between component oxides) which could stabilize certain highly useful, but also barely accessible phases under ambient conditions.<sup>19</sup> All these demonstrate a great possibility of using interfacial dislocations or strains in developing symbiotic hetero-nanocomposites that

<sup>a</sup>State Key Laboratory of Inorganic Synthesis and Preparative Chemistry, College of Chemistry, Jilin University, Changchun 130012, P. R. China. E-mail: [lipingli@jlu.edu.cn](mailto:lipingli@jlu.edu.cn)

<sup>b</sup>Institute of Chemical and Engineering Sciences, A\*STAR, 1 Pesek Road, Jurong Island, Singapore 627833, Singapore

<sup>c</sup>State Key Laboratory of Supramolecular Structure and Materials, College of Chemistry, Jilin University, Changchun 130012, P. R. China

† Electronic supplementary information (ESI) available. See DOI: [10.1039/c9sc01216h](https://doi.org/10.1039/c9sc01216h)



contain unachievable phases for many important applications, which however remains a significant challenge owing to the tedious formation conditions (like pre-synthesis and post-processing) and the need for precise control over atomic nucleation in synthetic chemistry. Consequently, it is highly necessary to explore one-step approaches for synthesizing symbiotic hetero-nanocomposites *via* precise control over the composition intergrowth during the nucleation and crystallization process.

Depending on the synthetic chemistry, symbiotic hetero-nanocomposites could be achieved in many classes of oxide systems because of the intrinsic nature of polymorphs. For instance,  $\text{TiO}_2$  has many crystalline phases. Heterogeneous composites formed in between rutile, anatase, and/or brookite-type  $\text{TiO}_2$  have been evidenced (*e.g.*, anatase/rutile, anatase/brookite, rutile/brookite or anatase/rutile/brookite) to show strong interfacial interactions because of the intergrowth of these phases during the synthesis of  $\text{TiO}_2$ . Closely related to the specific combination of these constituent structures, heterogeneous composites have found a broad range of applications such as in photocatalysis, lithium-ion batteries, CO oxidation, and ammonia synthesis.<sup>17,20–22</sup> P25 is a typical heterogeneous composite that consists of anatase and rutile at a molar ratio of 79 to 21, and has shown a preeminent performance in photocatalytic hydrogen production and sewage treatment. Indeed, the intergrowth compositions of  $\text{TiO}_2$  are rather limited to those of common phases, while heterogeneous composites that involve many other unconventional phases of  $\text{TiO}_2$  (like  $\text{TiO}_2\text{-H}$ ,  $\text{CaCl}_2$  phase, or  $\alpha\text{-PbO}_2$  phase, *etc.*) are barely accessible. This is because the synthesis of these unconventional phases can only be achieved under harsh experimental conditions such as high pressure and high temperature, even though these phases have been predicted to have superior activity in batteries and photocatalysis.<sup>23,24</sup> Consequently, an intergrowth of heterogeneous composites with those unconventional phases is highly important, but also fairly challenging.

We hold the opinion that the  $\text{CaCl}_2$  phase and rutile could most probably form a symbiotic hetero-nanocomposite with a broad impact if successful. We took  $\text{CaCl}_2$ /rutile as the target to study based on the following considerations: (i) among all unconventional phases of  $\text{TiO}_2$ , the orthorhombic  $\text{CaCl}_2$ -type  $\text{TiO}_2$  polymorph with a space group of  $Pnnm$  is a distorted structure of tetragonal rutile with a relative tilt of adjacent ribbons about the *c*-axis, whose structure is very close but absolutely different from rutile. They are likely to connect with each other and grow together through orientation attachment, leading to dislocations in between them that could in turn stabilize this metastable phase; (ii) although the  $\text{CaCl}_2$  phase can only be synthesized under high pressure by assistance of foreign ions currently,<sup>25,26</sup> solution chemistry especially the hydrothermal approach merited by a special subcritical reaction medium and abundant intermediate states could regulate the flexible reaction procedure to obtain several special phases with a metastable structure. Further, hydrothermal methods allow control over the nucleation and growth processes essential for synthesizing symbiotic hetero-nanocomposites with strong interactions.<sup>27</sup> (iii) There are many other rutile counterparts like  $\text{SnO}_2$ ,  $\text{SiO}_2$ ,  $\text{GeO}_2$ , and  $\text{RuO}_2$  that have been found to transform

into the  $\text{CaCl}_2$  structure under high pressure.<sup>28–31</sup> Thus, once such a solution methodology was established, one may expect more opportunities to develop other  $\text{CaCl}_2$ /rutile symbiotic hetero-nanocomposites. As we all know, rutile is an excellent multi-functional material in a wide range of fields, and thus it is highly possible for symbiotic hetero-nanocomposites with a distorted rutile structure to show superior performances that have not yet been accessible.

Herein, we successfully synthesized a symbiotic hetero-nanocomposite that consists of metastable  $\text{CaCl}_2$  structured  $\text{TiO}_2$  and rutile  $\text{TiO}_2$  *via* a mild solution chemistry approach. The composite structure of symbiotic  $\text{CaCl}_2$ /rutile  $\text{TiO}_2$  was confirmed by XRD data refinement, EXAFS, and Raman spectra. Then, the phase diagram for the symbiotic hetero-nanocomposite was depicted based on the reactant concentration and reaction temperature, in which the  $\text{Ti}(\text{OH})_2(\text{OH}_2)_4^{2+}$  saturation ion played a crucial role. Despite the presence of metastable  $\text{CaCl}_2$  structured  $\text{TiO}_2$ , the as-prepared hetero-nanocomposite showed a high stability and a superior performance in photocatalytic  $\text{H}_2$  evolution reactions through forming a type II heterojunction. This work provides insights into developing new methods for synthesizing high-performance symbiotic hetero-nanocomposites that contain metastable compounds.

## Results and discussion

Titania polymorphs in this work were synthesized through a high-acidity hydrothermal process utilizing  $\text{TiCl}_4$  as the titanium source, and no other reagents were needed except for the aqueous solution. After reaction at 120 °C for 2 h, the product was examined by powder X-ray diffraction (XRD) to identify the structure. As shown in Fig. 1c, the XRD data of the product were readily indexed to a rutile phase of  $\text{TiO}_2$  in tetragonal structure (JCPDS no. 21-1276). However, unlike the traditional rutile  $\text{TiO}_2$ , the diffraction line (110) around two theta of 28° is clearly asymmetric (Fig. 1a). This diffraction peak could be fitted well using two Lorentz fitting peaks: one shifted towards a higher diffraction angle, while the other one shifted oppositely and became symmetric gradually after calcination at 200 °C and 400 °C (Fig. S1† and 1b). Typically, the origins of the doublet peaks are regarded as  $\text{K}_{\alpha 1}$  and  $\text{K}_{\alpha 2}$  rays of the Cu target during XRD measurements. However, the peak splitting caused by the Cu target couldn't be so large.<sup>32</sup> Thus, the influence of the instrument was excluded, and the peak splitting around two theta of 28° could be attributed to the change of the structure. To the best of our knowledge, the peak splitting of diffraction peaks could be the consequences of (i) strain; for instance, polymer capping induced strain may result in changes in the lattice constant, and crystal boundary strain in the twin crystal could give rise to doublet XRD peaks;<sup>33–35</sup> (ii) surface species, such as water vapour on the surface of ice;<sup>36</sup> and (iii) distortion of the structure.<sup>37</sup> Asymmetry of diffraction peaks induced by strain and surface species is often composed of one strong intrinsic peak accompanied by weak peaks at the shoulder, differing from two comparative peaks. The sole possibility is appearance of the composition in a new phase. Firstly, we assumed that the



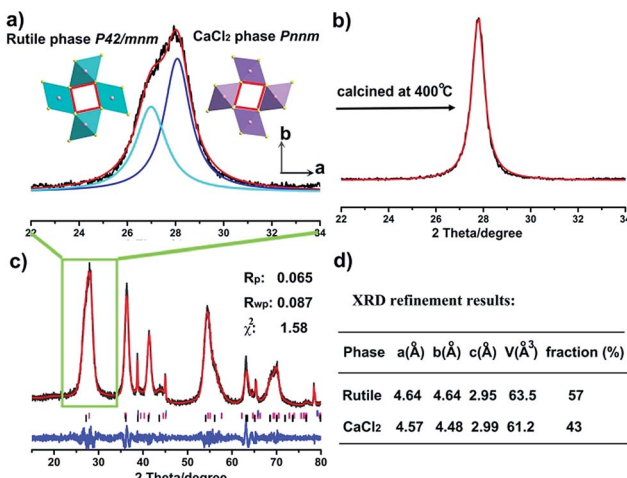


Fig. 1 Structural analyses by X-ray diffraction (XRD) refinement: (a) XRD pattern of the enlarged peak (110) for  $CaCl_2$ /rutile  $TiO_2$ . Inset illustrates the crystal structures for rutile  $TiO_2$  and  $CaCl_2$  phase  $TiO_2$ . (b) XRD pattern of the calcined product  $CaCl_2$ /rutile-400. (c) Rietveld structural data refinement results for  $CaCl_2$ /rutile  $TiO_2$ . Black, red, and blue curves represent the experimental diffraction data, calculated data, and deviation between the experimental and calculated data, respectively. The vertical bars below the pattern denote the standard diffraction data for internal standard Al (blue), rutile  $TiO_2$  (black) and  $CaCl_2$  phase  $TiO_2$  (rose red). (d) The structural refinement results for components rutile and  $CaCl_2$  in the composite.

peak splitting originates from two rutile  $TiO_2$  phases intergrown with a shrinking lattice and an expanded lattice. That is, two tetragonal  $TiO_2$  structures with space group of  $P4_2/mnm$  coexist in this material. Thus, according to eqn (S1),<sup>†</sup> two sets of lattice parameters could be obtained when calculated using  $d$  values of peaks (110) and (101), as shown in Table S1.<sup>†</sup> The lattice volume obtained from the left peak (peak 1) is well consistent with the experimental curve of  $V-1/D$  of rutile  $TiO_2$ , while the lattice volume obtained from the right peak (peak 2) severely deviates from the curve (Fig. S2<sup>†</sup>), giving a hint that peak 2 does not originate from rutile  $TiO_2$  with a contracted lattice. This means that one has to look for other structured  $TiO_2$  similar to rutile. Coincidentally, a similar phenomenon has been found in rutile  $SnO_2$  under a pressure of 250 bar, and the author assigned the structure to a  $CaCl_2$  structure (space group  $Pnnm$ ) that forms through a second-order phase transition from the rutile phase.<sup>38</sup> Typically, the  $CaCl_2$  structure is an orthorhombic structure that occurs at a very high pressure, which has been found in many rutile structured compounds including  $SnO_2$ ,  $SiO_2$ ,  $GeO_2$ ,  $RuO_2$ ,  $TiO_2$ , etc.<sup>25,28–31</sup> It seems reasonable that there is a  $CaCl_2$  phase in the as-prepared  $TiO_2$ , which explains the peak splitting around

two theta of 28° in Fig. 1a. Thus, the XRD patterns were fitted in terms of rutile and  $CaCl_2$  structure. As one expected, the results agree well with the data (Fig. 1, Tables 1, S2 and S3<sup>†</sup>). The lattice parameters of the  $CaCl_2$  structure in  $CaCl_2$ /rutile  $TiO_2$  were determined to be  $a = 4.57 \text{ \AA}$ ,  $b = 4.48 \text{ \AA}$ ,  $c = 2.99 \text{ \AA}$ . It is authentic to identify the existence of  $CaCl_2$ -type structured  $TiO_2$  in  $CaCl_2$ /rutile  $TiO_2$ .

In order to further verify our speculation,  $CaCl_2$ /rutile  $TiO_2$  was further characterized by field-emission scanning electron microscopy (SEM) and transmission electron microscopy (TEM) which display a cone shape at a dimension of about 2–3  $\mu\text{m}$  (Fig. 2b and S6<sup>†</sup>). The cone was composed of numerous nanorods with a width of about 5 nm grouped by small nanoparticles through orientation attachment growth. High resolution transmission electron microscopy (HRTEM) indicates that the lattice spacing is ordered locally, while the lattice parameters vary in different parts (Fig. 2c, f and g). The interplanar spacing ( $d$ ) in different parts of Fig. 2c differ (such as  $d_1 = 0.320 \text{ \AA}$ ,  $d_2 = 0.328 \text{ \AA}$ ), which are in accordance with the plane (110) in rutile and  $CaCl_2$  structure from the refinement results of  $CaCl_2$ /rutile  $TiO_2$  (Table 1). Besides that, there are a large number of dislocations in the joint point of both parts (Fig. 2c). Benefiting from the dislocation, the neighbouring particles attached to each other and tended to grow together, as illustrated in the schematic diagram in Fig. 2a. Thus, the formation of  $CaCl_2$ -type structured  $TiO_2$  intergrown with rutile  $TiO_2$  was confirmed.

When the intergrowth structure was calcined at high temperatures, the lattice tends to be regular and transformed entirely into a rutile  $TiO_2$  phase with a little shrinkage relative to the rutile phase in  $CaCl_2$ /rutile  $TiO_2$ . This observation is likely due to the phase transition of the metastable  $CaCl_2$  structure to the rutile structure and the growth of crystals. The  $d$  spacing could be identified to decrease to a value of 0.325  $\text{\AA}$  from HRTEM, which is also consistent with XRD refinement results of  $CaCl_2$ /rutile-400 and commercial rutile (Fig. S3 and S4, Tables S4 and S5<sup>†</sup>). It should be mentioned that uniform mesopores ( $\sim 8 \text{ nm}$ ) appeared with the cone-shape maintained after calcination (Fig. 2d and S6b<sup>†</sup>), in line with the pore distributions obtained by  $N_2$  adsorption/desorption isotherm curves (Fig. S5<sup>†</sup>). Lattice rearrangement should be responsible for the appearance of mesopores. As the calcination temperature increased, the specific areas decreased (Table S6<sup>†</sup>) due to the grain growth.

The Raman spectrum is often used as a fingerprint to analyze the symmetry and structural order. As shown in Fig. 3a, three signals located at about 140, 400, and 600  $\text{cm}^{-1}$  are associated with the modes  $B_{1g}$ ,  $E_g$ , and  $A_{1g}$  of the rutile  $TiO_2$  lattice,

Table 1 XRD refinement results of the samples

Sample name (phase)	Lattice	Space group	$a/\text{\AA}$	$b/\text{\AA}$	$c/\text{\AA}$	$V/\text{\AA}^3$	$d(110)/\text{\AA}$	$\chi^2$
$CaCl_2$ /rutile $TiO_2$ ( $CaCl_2$ phase)	Orthorhombic	$Pnnm$	4.569	4.484	2.988	61.21	3.200	1.575
$CaCl_2$ /rutile $TiO_2$ (rutile phase)	Tetragonal	$P4_2/mnm$	4.642	4.642	2.947	63.51	3.283	
$CaCl_2$ /rutile-400 (rutile phase)	Tetragonal	$P4_2/mnm$	4.596	4.596	2.957	62.46	3.250	5.513
Ref. $TiO_2$ (rutile phase)	Tetragonal	$P4_2/mnm$	4.593	4.593	2.958	62.42	3.248	2.542



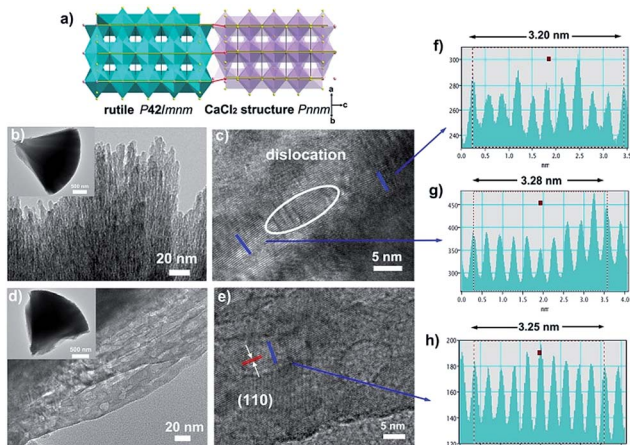


Fig. 2 Morphology and assembly structure of the composite: (a) schematic diagram of the assembly structure, (b) TEM and (c) HRTEM images for  $\text{CaCl}_2$ /rutile  $\text{TiO}_2$ , (d) TEM and (e) HRTEM images for  $\text{CaCl}_2$ /rutile-400. Profiles of lattice fringes for (f and g)  $\text{CaCl}_2$ /rutile  $\text{TiO}_2$  in different areas; and (h) profiles of lattice fringe for  $\text{CaCl}_2$ /rutile-400. Scale value in insets of (b) and (d) are 500 nm.

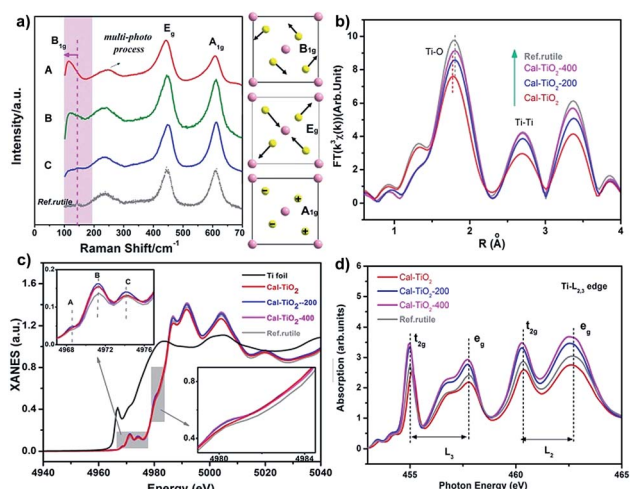


Fig. 3 Structural information from Raman and EXAFS. (a) Raman spectra, (b)  $R$ -space Fourier-transformed FT ( $k^3\chi(k)$ ) of Ti K-edge EXAFS, (c) XANES spectra of the Ti K-edge and (d) Ti  $L_{2,3}$ -edge of the samples  $\text{CaCl}_2$ /rutile  $\text{TiO}_2$  (A),  $\text{CaCl}_2$ /rutile-200 (B),  $\text{CaCl}_2$ /rutile-400 (C) and commercial rutile  $\text{TiO}_2$ . The gray area in (c) highlights the pre-edge region.

respectively, while that at  $200\text{ cm}^{-1}$  can be assigned to the multi-phonon modes of rutile  $\text{TiO}_2$ .<sup>39,40</sup> It should be pointed out that in  $\text{CaCl}_2$ /rutile  $\text{TiO}_2$ , a weak signal of the  $B_{1g}$  mode for rutile  $\text{TiO}_2$  at  $140\text{ cm}^{-1}$  became inconspicuous and overlapped by a new peak at about  $110\text{ cm}^{-1}$ . In Raman active modes of rutile, the central cation Ti is silent, and the Raman modes are purely O vibrations.<sup>39</sup> As shown in the schematic diagram in Fig. 3a, the oxygen ions vibrate perpendicular to the Ti–O bond in the  $B_{1g}$  mode. Typically, the  $B_{1g}$  mode is highly sensitive to the long-range order of  $\text{TiO}_2$  crystals and softens significantly more than other modes under high pressures.<sup>41</sup> The Raman shift in rutile

often has a relationship with the strain, O/Ti ratio, size effect, O isotope, and volume effect, which usually give rise to several wavenumber shifts.<sup>39,40,42,43</sup> The most significant factor could be the pressure-induced-volume effect as represented by a shift of about  $20\text{ cm}^{-1}$  softened at 6 GPa.<sup>40</sup> Several viewpoints have attributed the origin of anomalistic softening in the  $B_{1g}$  mode to a thermal/pressure-induced-lattice contraction or an incipient structural phase transition, which explains well the softening of mode  $B_{1g}$ . Thus, the new emerging peak at  $110\text{ cm}^{-1}$  most likely originates from  $\text{CaCl}_2$  structured  $\text{TiO}_2$  in  $\text{CaCl}_2$ /rutile  $\text{TiO}_2$ . Due to the intense signal of this vibration, the intrinsic signal for rutile is covered by that of  $\text{CaCl}_2$  phase  $\text{TiO}_2$ .

In order to investigate the coordination environment of  $\text{CaCl}_2$ /rutile  $\text{TiO}_2$ , Ti K-edge X-ray adsorption spectra of  $\text{CaCl}_2$ /rutile  $\text{TiO}_2$  and its calcined samples were measured and compared. As shown in Fig. 3b, Ti K-edge EXAFS of  $\text{CaCl}_2$ /rutile  $\text{TiO}_2$ ,  $\text{CaCl}_2$ /rutile-200,  $\text{CaCl}_2$ /rutile-400, and commercial rutile  $\text{TiO}_2$  (Ref.rutile) are transformed into the radial distribution function *via*  $R$ -space Fourier-transformed FT ( $k^3\chi(k)$ ). The first peak at about  $1.8\text{ \AA}$  is attributed to the six Ti–O bonds in the first coordination sphere ( $\text{TiO}_6$  octahedron) and the second peak at about  $2.7\text{ \AA}$  could be ascribed to Ti–Ti distances of these samples. The third peak at  $3.4\text{ \AA}$  corresponds to Ti–O bonds at about  $3.5\text{ \AA}$  and Ti–Ti bonds at  $3.57\text{ \AA}$ . Obviously, the Ti–O distance in  $\text{CaCl}_2$ /rutile  $\text{TiO}_2$  is shorter than those of other samples, which could be caused by  $\text{CaCl}_2$ -type structured  $\text{TiO}_2$  with a contracted unit cell. Normalized Ti K-edge XANES spectra are shown in Fig. 3c. The line shape of  $\text{CaCl}_2$ /rutile  $\text{TiO}_2$ ,  $\text{CaCl}_2$ /rutile-200 and  $\text{CaCl}_2$ /rutile-400 is similar to that of commercial rutile  $\text{TiO}_2$  except for a subtle change in the relative intensities of peaks and the absorption edge. The three major features in the pre-peaks of the Ti K-pre-edge region are labelled A, B, and C, which are identified to be associated with hybridized Ti 3d–4p, and  $1s \rightarrow 2t_{2g}$  and  $1s \rightarrow 3e_g$  transitions, respectively.<sup>44,45</sup> The intensity of pre-peak B in  $\text{CaCl}_2$ /rutile  $\text{TiO}_2$ ,  $\text{CaCl}_2$ /rutile-200, and  $\text{CaCl}_2$ /rutile-400 is stronger than that of commercial rutile  $\text{TiO}_2$ . It is well established that the intensity of pre-peak B enhanced with increasing concentration of defects.<sup>45,46</sup> Oxygen vacancy signals were then detected by ESR at  $g = 2.00$  (Fig. S7†),<sup>47</sup> the calcined samples showed obvious signals of oxygen vacancies, whereas,  $\text{CaCl}_2$ /rutile  $\text{TiO}_2$  did not show any single electron signal ( $\text{Ti}^{3+}$  or single electron trapped in oxygen vacancies), indicating the absence of defect sites in  $\text{CaCl}_2$ /rutile  $\text{TiO}_2$ . Even so, there are dislocations (line defects) in  $\text{CaCl}_2$ /rutile  $\text{TiO}_2$ , which should be responsible for the enhanced pre-peak B. Another change in normalized Ti K-edge XANES spectra is the absorption edge. It is easy to understand why the lower absorption edge energy of calcined samples stems from the existence of  $\text{Ti}^{3+}$ , while, the inconformity of the absorption edge of  $\text{CaCl}_2$ /rutile  $\text{TiO}_2$  cannot be explained in terms of valence characteristics of Ti ions. Instead, the covalency in  $\text{CaCl}_2$ /rutile  $\text{TiO}_2$  was enhanced due to the shortened Ti–O distance.

In addition, Ti  $L_{2,3}$ -edge absorption spectra are also measured to study the electronic structure, as shown in Fig. 3d. Two sets of local maxima over this energy range could be assigned to Ti  $2p_{3/2}$  ( $L_3$ : peaks  $t_{2g}$  and  $e_g$ ) and Ti  $2p_{1/2}$  ( $L_2$ : peaks  $t_{2g}$  and  $e_g$ ) core levels into empty Ti 3d states.<sup>48,49</sup> It should be



noted that the difference value ( $\Delta E$ ) of peaks  $t_{2g}$  ( $L_3$ ) to  $e_g$  ( $L_3$ ) of  $\text{CaCl}_2$ /rutile  $\text{TiO}_2$  decreases compared with other samples, which is caused by the lattice distortion of rutile  $\text{TiO}_2$ .

It is well known that the formation of  $\text{TiO}_2$  in different phases (like rutile, anatase, and brookite) proceeds under specific conditions, and these phases often transform into each other through external energy, as previously reported.<sup>50,51</sup> However,  $\text{CaCl}_2$  structured  $\text{TiO}_2$  has not been obtained under mild conditions and the formation inducement has not been uncovered. Herein, we initiated experiments under a broad range of conditions with varying the amount of reactants and reaction temperature with an aim to obtain the phase diagram for given phases and nanostructures (Fig. 4a, S8 and S9†). It seems that solution reaction with a high concentration of  $\text{TiCl}_4$  leads to the occurrence of  $\text{CaCl}_2$ -type structured  $\text{TiO}_2$ , while a low concentration of  $\text{TiCl}_4$  causes an appearance of the anatase phase. In the boundary of the  $\text{CaCl}_2$  phase and anatase phase, pure rutile formed. With increasing the amount of  $\text{TiCl}_4$ , no products could be obtained except for a solution. Through this mapping, we didn't find an indication that pure  $\text{CaCl}_2$  phase  $\text{TiO}_2$  is formed through the hydrolytic process of  $\text{TiCl}_4$ . This may be due to the metastable structure of  $\text{CaCl}_2$  phase  $\text{TiO}_2$ , which makes it hard to stabilize by itself. Further, the symbiotic structure is vital in stabilizing the metastable  $\text{CaCl}_2$  phase  $\text{TiO}_2$ . Based on the synthetic maps, the possible formation process of  $\text{CaCl}_2$ /rutile  $\text{TiO}_2$  was proposed in terms of the schematic diagram in Fig. 4b: when the starting reactant

$\text{TiCl}_4$  was dissolved in water, water-soluble precursor  $\text{Ti}(\text{OH})_2(\text{OH}_2)_4\text{Cl}_2$  was formed initially, and the solution became highly acidic. Then, the precursor was dissociated and condensed to crystallize  $\text{TiO}_2$  through an oxolation. At a high concentration of  $\text{TiCl}_4$ ,  $\text{Ti}(\text{OH})_2(\text{OH}_2)_4\text{Cl}_2$  could not be completely disintegrated to create a crystalline  $\text{TiO}_2$  phase,<sup>52</sup> leaving lots of redundant saturation  $\text{Ti}(\text{OH})_2(\text{OH}_2)_4^{2+}$  ions and  $\text{Cl}^-$  ions scattered around the crystals that affect the crystallization and the subsequent grain growth process. Even after the reaction, there remained a great number of  $\text{Ti}(\text{OH})_2(\text{OH}_2)_4^{2+}$  ions in the solution. In order to verify the existence of soluble titanium compounds, the filter liquor was collected. At first, ultra-pure  $\text{H}_2\text{O}$  was added, the solution showed a phenomenon of liquid miscibility with visible flow traces, and no precipitates appeared, which is due to the large viscosity and mobility difference between  $\text{H}_2\text{O}$  and the filter liquor with a high concentration of  $\text{Ti}(\text{OH})_2(\text{OH}_2)_4^{2+}$ . Then, excessive  $\text{NaOH}$  was put in and plenty of white precipitates appeared which indicates the presence of titanium compounds in this filter liquor. This observation shows that a high concentration of  $\text{Ti}(\text{OH})_2(\text{OH}_2)_4^{2+}$  ions plays an important role in the formation of symbiotic  $\text{CaCl}_2$ /rutile  $\text{TiO}_2$ . Similar cases have been reported elsewhere, in which ions can regulate the morphology and structure of final products.<sup>53,54</sup>

The stability of  $\text{CaCl}_2$ /rutile  $\text{TiO}_2$  was measured using *in situ* XRD through increasing the temperature gradually. The double peak feature of plane (110) is still clear when calcined at temperatures  $<200$  °C, and then fades away as the calcination temperature increases (Fig. 5a). Meanwhile, such a feature remains unchanged if the samples are kept at room temperature for as long as three years (Fig. 5c), suggesting a good stability. Clearly, in the phase transition process, the double peaks located at two theta of about 27.0° and 27.9° gradually change into a single peak at two theta of about 27.5° (Fig. 5b). This reflects the lattice change process more intuitively: the  $\text{CaCl}_2$  phase fades away little by little, and the rutile phase contracts in the lattice with grain growth.

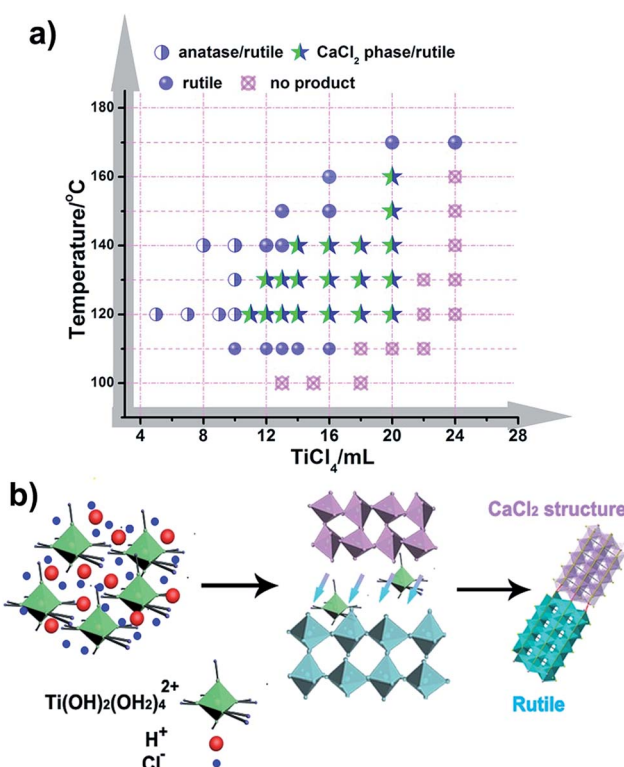


Fig. 4 Chemical synthesis routes. (a) Maps for the synthesis of  $\text{TiO}_2$  at various hydrothermal temperatures and addition amounts of  $\text{TiCl}_4$ . (b) The synthetic schematic diagram for the formation of  $\text{CaCl}_2$ /rutile  $\text{TiO}_2$ .

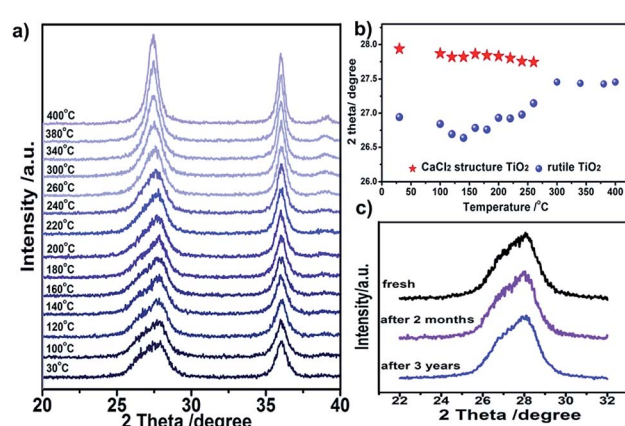


Fig. 5 Stability of symbiotic  $\text{CaCl}_2$ /rutile  $\text{TiO}_2$ . (a) *In situ* XRD patterns for  $\text{CaCl}_2$ /rutile  $\text{TiO}_2$  with increasing temperature from 30 to 400 °C. (b) Peak position variation as temperature increases. (c) XRD patterns for fresh  $\text{CaCl}_2$ /rutile  $\text{TiO}_2$  and the samples after being stored in air for two months and three years as well.



It is well known that hetero-nanocomposites of  $\text{TiO}_2$  like P25 are excellent photocatalysts, however, no one knows what the performance is for symbiotic hetero-nanocomposite  $\text{CaCl}_2$ /rutile  $\text{TiO}_2$ . Since the band structure of  $\text{CaCl}_2$ -type  $\text{TiO}_2$  directly determines its photocatalytic activity, we calculated the density of states (DOS) of  $\text{CaCl}_2$  phase  $\text{TiO}_2$  and rutile  $\text{TiO}_2$  in  $\text{CaCl}_2$ /rutile  $\text{TiO}_2$  (Fig. 6a). The conduction band minimum of both materials originates from the Ti 3d orbital, and the valence band maximum consists mainly of the O 2p orbital. Nevertheless, the band gap energy of  $\text{CaCl}_2$  structured  $\text{TiO}_2$  ( $E_g \approx 3.3$  eV) is obviously larger than that of rutile  $\text{TiO}_2$  ( $E_g \approx 3.1$  eV). The origin of the difference in band structure lies in the unique features of  $\text{CaCl}_2$  phase  $\text{TiO}_2$ , which owns an entirely different octahedral configuration and Ti–O bond length when compared to rutile  $\text{TiO}_2$ . The change in bond length could affect the interaction between orbitals, leading to variations in the band position.<sup>55</sup> Experimentally, we measured the diffuse reflectance ultraviolet-visible spectra and XPS valence band spectra. The absorbance range of  $\text{CaCl}_2$ /rutile  $\text{TiO}_2$  is similar to that of rutile  $\text{TiO}_2$  ( $E_g \approx 3.1$  eV) except for an enhanced absorption intensity

around 360 nm (Fig. S10†). Combined with the DOS analysis results in which the band gap of  $\text{CaCl}_2$  phase  $\text{TiO}_2$  is wider than that of rutile  $\text{TiO}_2$ , we could attribute the enhanced light absorption near 360 nm to the electron excitation from the O 2p orbital to the Ti 3d orbital of the  $\text{CaCl}_2$  phase  $\text{TiO}_2$ . The edge absorption around 400 nm primarily originates from electron excitation from the O 2p orbital to the Ti 3d orbital of rutile  $\text{TiO}_2$ . From XPS spectra in Fig. S11,† the valence band of  $\text{CaCl}_2$ /rutile  $\text{TiO}_2$  is determined to be about 0.2 eV lower than that of rutile  $\text{TiO}_2$  ( $E_{\text{VBM}}^{\text{rutile}} = 2.62$  eV,  $E_{\text{VBM}}^{\text{CaCl}_2/\text{rutile}} = 2.44$  eV). Thus,  $\text{CaCl}_2$ /rutile  $\text{TiO}_2$  forms a type II heterojunction similar to that of P25, as illustrated in the schematic diagram (Fig. 6f). Photoexcited charges would transport and accumulate in semiconductors.<sup>56,57</sup> That is, photo-generated electrons in  $\text{CaCl}_2$  structured  $\text{TiO}_2$  could transport to rutile  $\text{TiO}_2$  preferentially to conduct reduction reactions. Meanwhile, the holes left in the valence of rutile  $\text{TiO}_2$  would transport to  $\text{CaCl}_2$  structured  $\text{TiO}_2$  preferentially to react with the sacrificial agent.

The charge separation and transport efficiency were evaluated through electrochemical impedance measurements (EIS). As shown in Fig. 6b, the arc in the low-frequency range originates from electron transfer resistance ( $R_t$ ). Obviously, the arc of  $\text{CaCl}_2$ /rutile  $\text{TiO}_2$  is smaller than those of Ref.  $\text{TiO}_2$  and P25, indicating a more rapid electron transfer process in  $\text{CaCl}_2$ /rutile  $\text{TiO}_2$ . As expected, the as-prepared  $\text{CaCl}_2$ /rutile  $\text{TiO}_2$  exhibits a superior performance in mass-specific  $\text{H}_2$  evolution ( $1024 \mu\text{mol g}^{-1} \text{h}^{-1}$ ) to rutile  $\text{TiO}_2$  ( $174 \mu\text{mol g}^{-1} \text{h}^{-1}$ ), and a comparable performance with P25 ( $1019 \mu\text{mol g}^{-1} \text{h}^{-1}$ ) under AM 1.5G simulated sunlight with the assistance of 1% Pt cocatalyst (Fig. 6e). It is well known that P25 is an excellent ultraviolet light absorber, while its visible light absorbance ability is low. Comparatively, the absorption edge of  $\text{CaCl}_2$ /rutile  $\text{TiO}_2$  showed an obvious red shift compared with P25, which means that  $\text{CaCl}_2$ /rutile  $\text{TiO}_2$  owns a wider range of light absorption (Fig. S10†). Besides this, dislocations that involve defects and/or local disorder may provide a mid-gap state in  $\text{CaCl}_2$ /rutile  $\text{TiO}_2$  to broaden the light absorption range.<sup>58</sup> Thus, under visible light illumination ( $\lambda > 400$  nm),  $\text{CaCl}_2$ /rutile  $\text{TiO}_2$  exhibited the highest  $\text{H}_2$  evolution activity ( $177 \mu\text{mol g}^{-1} \text{h}^{-1}$ ), much higher than that of commercial rutile  $\text{TiO}_2$  ( $23 \mu\text{mol g}^{-1} \text{h}^{-1}$ ) and P25 ( $42 \mu\text{mol g}^{-1} \text{h}^{-1}$ ) (Fig. 6d). Surprisingly, without the assistance of a cocatalyst,  $\text{CaCl}_2$ /rutile  $\text{TiO}_2$  still showed the most outstanding performance under the illumination of simulated sunlight (Fig. 6c), which also indicates the excellent charge separation ability of symbiotic  $\text{CaCl}_2$ /rutile  $\text{TiO}_2$ . The cycle tests of  $\text{CaCl}_2$ /rutile  $\text{TiO}_2$  for photocatalytic  $\text{H}_2$  generation proved a high stability in performance (Fig. S12†), which is further confirmed by the maintained structural feature after photocatalytic tests (Fig. S13†). Such an excellent performance can be primarily attributed to (i) the special structure of  $\text{CaCl}_2$ -phase  $\text{TiO}_2$  which provides the  $\text{CaCl}_2$ /rutile  $\text{TiO}_2$  hetero-nanocomposite with a higher reduction ability, and (ii) the symbiotic relationship that allows the  $\text{CaCl}_2$ /rutile  $\text{TiO}_2$  hetero-nanocomposite to show a strong interaction, which could separate and transport carriers efficiently.

$\text{TiO}_2$  is a multipurpose material, and many efforts have been made investigating the microwave absorption and terahertz

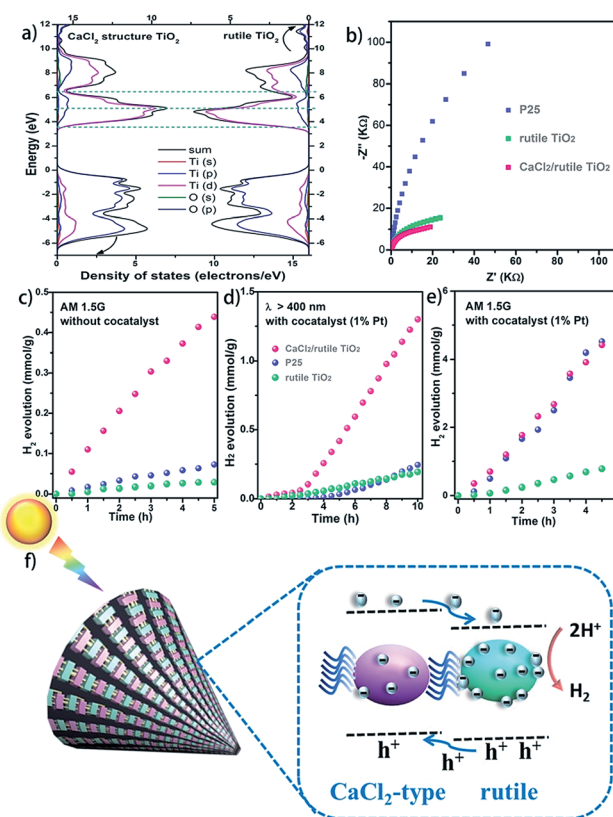


Fig. 6 Photocatalytic performance of  $\text{CaCl}_2$ /rutile  $\text{TiO}_2$ . (a) Calculated density of states (DOS) of  $\text{CaCl}_2$  structured  $\text{TiO}_2$  and rutile  $\text{TiO}_2$ ; (b) Nyquist plots of the EIS for  $\text{CaCl}_2$  structured  $\text{TiO}_2$ , P25, and commercial rutile  $\text{TiO}_2$  (Ref.rutile); Water splitting hydrogen evolution activities for  $\text{CaCl}_2$ /rutile  $\text{TiO}_2$ , commercial rutile  $\text{TiO}_2$  (Ref.rutile), and P25: (c) without any cocatalyst under simulated sunlight (with an AM 1.5G filter), (d) with the assistance of 1% Pt as the cocatalyst under simulated sunlight (with an AM 1.5G filter) and (e) visible light (wavenumber  $> 400$  nm) illumination. (f) Schematic diagram for the electron transfer process under the illumination of light for  $\text{CaCl}_2$ /rutile  $\text{TiO}_2$ .



absorption performance of hydrogenated  $\text{TiO}_2$ .<sup>59,60</sup> Thus, we examined the microwave absorption performance (1–18 GHz) of  $\text{CaCl}_2$ /rutile  $\text{TiO}_2$ , Ref. $\text{TiO}_2$  and P25 (Fig. S14 and S15†). Compared with Ref. $\text{TiO}_2$  and P25,  $\text{CaCl}_2$ /rutile  $\text{TiO}_2$  improved the reflection loss or absorption of the microwave irradiation (see details in the ESI†). This is likely from the existence of  $\text{CaCl}_2$  phase  $\text{TiO}_2$ . There are also many other potential applications worth studying, and the symbiotic  $\text{CaCl}_2$ /rutile  $\text{TiO}_2$  hetero-nanocomposite is believed to be a promising candidate in other areas.

## Conclusions

We report the synthesis of a symbiotic  $\text{CaCl}_2$ /rutile  $\text{TiO}_2$  hetero-nanocomposite through a facile hydrothermal approach. The successful synthesis relies on the existence of high concentration  $\text{Ti}(\text{OH})_2(\text{OH}_2)_4^{2+}$ , which affects nucleation and crystallization behaviour, resulting in the formation of  $\text{CaCl}_2$  structured  $\text{TiO}_2$  intergrown with rutile  $\text{TiO}_2$ . In this composite, orthorhombic  $\text{CaCl}_2$  phase  $\text{TiO}_2$  with a space group of  $Pnnm$  was stabilized by tetragonal phase rutile nanocrystals through dislocation connection in between both structures. Such a symbiotic relationship leads to a type II heterojunction, which enhances the charge separation and transport ability. The specific structure of  $\text{CaCl}_2$ /rutile  $\text{TiO}_2$  elevated the reduction capacity, enabling a superior photocatalytic water splitting activity higher than that of the most widely used photocatalyst P25. We believe that the synthesis of the symbiotic  $\text{CaCl}_2$ /rutile  $\text{TiO}_2$  hetero-nanocomposite reported here would facilitate its extensive research in those fields that have not yet been found and would provide guidance for the synthesis of other advanced hetero-nanocomposite materials.

## Conflicts of interest

The authors declare no competing financial interest.

## Acknowledgements

We acknowledge the technical assistance of the Beijing Synchrotron Radiation Facility (BSRF) and National Synchrotron Radiation Laboratory (NSRL), Hefei, China. We also thank Pro. Xiaolong Wang (Jilin University), Pro. Minqiang Wang (Xi'an Jiaotong University), Dr Song Xia (Xi'an Jiaotong University), and Dr Xiangli Che (Shanghai Institute of Silicate, Chinese Academy of Sciences) for their assistance with the measurement and analysis of microwave absorption. This research is supported by the financial assistance of NSFC (21671077, 21871106, 21571176, and 21771075) and Interdisciplinary Research Grant for PhDs of Jilin University (10183201816).

## Notes and references

1 C. Xia, Y. X. Cai, Y. Ma, B. Y. Wang, W. Zhang, M. Karlsson, Y. Wu and B. Zhu, *ACS Appl. Mater. Interfaces*, 2016, **8**, 20748–20755.

- 2 C. L. Tan and H. Zhang, *J. Am. Chem. Soc.*, 2015, **137**, 12162–12174.
- 3 H. Y. Wang, H. S. Yin, H. Huang, K. L. Li, Y. L. Zhou, G. I. N. Waterhouse, H. Lin and S. Y. Ai, *Biosens. Bioelectron.*, 2018, **108**, 89–96.
- 4 G. Chen, Y. Zhao, G. Fu, P. N. Duchesne, L. Gu, Y. Zheng, X. Weng, M. Chen, P. Zhang, C. W. Pao, J. F. Lee and N. Zheng, *Science*, 2014, **344**, 495–499.
- 5 B. Kong, J. Tang, Y. Zhang, T. Jiang, X. Gong, C. Peng, J. Wei, J. Yang, Y. Wang, X. Wang, G. Zheng, C. Selomulya and D. Zhao, *Nat. Chem.*, 2016, **8**, 171–178.
- 6 J. Cai, M. Wu, Y. Wang, H. Zhang, M. Meng, Y. Tian, X. Li, J. Zhang, L. Zheng and J. Gong, *Chem.*, 2017, **2**, 877–892.
- 7 X. Y. Zheng, C. K. Yang, X. H. Chang, T. Wang, M. Ye, J. Lu, H. H. Zhou, J. Zheng and X. G. Li, *Adv. Mater.*, 2018, **30**, 1704353.
- 8 D. Jung, L. M. A. Saleh, Z. J. Berkson, M. F. El-Kady, J. Y. Hwang, N. Mohamed, A. I. Wixtrom, E. Titarenko, Y. Shao, K. McCarthy, J. Guo, I. B. Martini, S. Kraemer, E. C. Wegener, P. Saint-Cricq, B. Ruehle, R. R. Langeslay, M. Delferro, J. L. Brosmer, C. H. Hendon, M. Gallagher-Jones, J. Rodriguez, K. W. Chapman, J. T. Miller, X. Duan, R. B. Kaner, J. I. Zink, B. F. Chmelka and A. M. Spokoyny, *Nat. Mater.*, 2018, **17**, 341–348.
- 9 M. Zhu, Z. Sun, M. Fujitsuka and T. Majima, *Angew. Chem., Int. Ed.*, 2018, **57**, 2160–2164.
- 10 Y. P. Zang, L. P. Li, Y. S. Xu, Y. Zuo and G. S. Li, *J. Mater. Chem. A*, 2014, **2**, 15774–15780.
- 11 B.-R. Wulan, S.-S. Yi, S.-J. Li, Y.-X. Duan, J.-M. Yan and Q. Jiang, *Appl. Catal., B*, 2018, **231**, 43–50.
- 12 Q. Li, F. Zhao, C. Qu, Q. Shang, Z. Xu, L. Yu, J. R. McBride and T. Lian, *J. Am. Chem. Soc.*, 2018, **140**, 11726–11734.
- 13 B. Dong, J. Cui, Y. Gao, Y. Qi, F. Zhang and C. Li, *Adv. Mater.*, 2019, e1808185.
- 14 X. Chen, L. Li, Y. Xu, Y. Zhang and G. Li, *RSC Adv.*, 2016, **6**, 995–1003.
- 15 Y. Suchorski, S. M. Kozlov, I. Bespalov, M. Datler, D. Vogel, Z. Budinska, K. M. Neyman and G. Rupprechter, *Nat. Mater.*, 2018, **17**, 519–522.
- 16 H. Jeong, J. Bae, J. W. Han and H. Lee, *ACS Catal.*, 2017, **7**, 7097–7105.
- 17 I. X. Green, W. Tang, M. Neurock and J. T. Yates Jr, *Science*, 2011, **333**, 736–739.
- 18 M. Shahidi, B. Pichler and C. Hellmich, *Acta Mech.*, 2016, **227**, 229–252.
- 19 V. Thery, A. Boulle, A. Crunteanu, J. C. Orlanges, A. Beaumont, R. Mayet, A. Mennai, F. Cosset, A. Bessaoudou and M. Fabert, *Phys. Rev. B*, 2016, **93**, 184106.
- 20 H. Liang, Q. Meng, X. Wang, H. Zhang and J. Wang, *ACS Appl. Mater. Interfaces*, 2018, **10**, 14145–14152.
- 21 H. Liu, W. Li, D. Shen, D. Zhao and G. Wang, *J. Am. Chem. Soc.*, 2015, **137**, 13161–13166.
- 22 M. M. Shi, D. Bao, B. R. Wulan, Y. H. Li, Y. F. Zhang, J. M. Yan and Q. Jiang, *Adv. Mater.*, 2017, **29**, 1606550.
- 23 J. C. Perez-Flores, C. Baehtz, A. Kuhn and F. Garcia-Alvarado, *J. Mater. Chem. A*, 2014, **2**, 1825–1833.



24 H. Razavi-Khosroshahi, K. Edalati, M. Hirayama, H. Emami, M. Arita, M. Yamauchi, H. Hagiwara, S. Ida, T. Ishihara, E. Akiba, Z. Horita and M. Fuji, *ACS Catal.*, 2016, **6**, 5103–5107.

25 A. Escudero, L. Delevoye and F. Langenhorst, *J. Phys. Chem. C*, 2011, **115**, 12196–12201.

26 A. Escudero and F. Langenhorst, *J. Solid State Chem.*, 2012, **190**, 61–67.

27 J. Zhang, L. P. Li, X. S. Huang and G. S. Li, *J. Mater. Chem.*, 2012, **22**, 10480–10487.

28 K. Suito, N. Kawai and Y. Masuda, *Mater. Res. Bull.*, 1975, **10**, 677–680.

29 Y. Tsuchida and T. Yagi, *nature*, 1989, **340**, 217–220.

30 J. Haines, J. M. Leger and C. Chateau, *Phys. Rev. B: Condens. Matter Mater. Phys.*, 2000, **61**, 8701–8706.

31 S. Ono and K. Mibe, *Phys. Rev. B: Condens. Matter Mater. Phys.*, 2011, **84**, 054114.

32 N. Stojilovic, *J. Chem. Educ.*, 2018, **95**, 598–600.

33 S. Pereira, M. R. Correia, E. Pereira, K. P. O'Donnell, R. W. Martin, M. E. White, E. Alves, A. D. Sequeira and N. Franco, *Mater. Sci. Eng., B*, 2002, **93**, 163–167.

34 M. J. Shearer, L. Samad, Y. Zhang, Y. Zhao, A. Puretzky, K. W. Eliceiri, J. C. Wright, R. J. Hamers and S. Jin, *J. Am. Chem. Soc.*, 2017, **139**, 3496–3504.

35 H. Huang, H. Jia, Z. Liu, P. Gao, J. Zhao, Z. Luo, J. Yang and J. Zeng, *Angew. Chem., Int. Ed.*, 2017, **56**, 3594–3598.

36 D. B. Varshney, J. A. Elliott, L. A. Gatlin, S. Kumar, R. Suryanarayanan and E. Y. Shalaev, *J. Phys. Chem. B*, 2009, **113**, 6177–6182.

37 J. Hafizovic, M. Bjorgen, U. Olsbye, P. D. C. Dietzel, S. Bordiga, C. Prestipino, C. Lamberti and K. P. Lillerud, *J. Am. Chem. Soc.*, 2007, **129**, 3612–3620.

38 K. M. Jensen, M. Christensen, P. Juhas, C. Tyrsted, E. D. Bojesen, N. Lock, S. J. Billinge and B. B. Iversen, *J. Am. Chem. Soc.*, 2012, **134**, 6785–6792.

39 O. Frank, M. Zukalova, B. Laskova, J. Kurti, J. Kolta and L. Kavan, *Phys. Chem. Chem. Phys.*, 2012, **14**, 14567–14572.

40 T. Lan, X. Tang and B. Fultz, *Phys. Rev. B: Condens. Matter Mater. Phys.*, 2012, **85**, 094305.

41 S. Zhou, E. Čižmár, K. Potzger, M. Krause, G. Talut, M. Helm, J. Fassbender, S. A. Zvyagin, J. Wosnitza and H. Schmidt, *Phys. Rev. B: Condens. Matter Mater. Phys.*, 2009, **79**, 113201.

42 J. C. Parker and R. W. Siegel, *Appl. Phys. Lett.*, 1990, **57**, 943–945.

43 V. Swamy, *Phys. Rev. B: Condens. Matter Mater. Phys.*, 2008, **77**, 195414.

44 C. Ribeiro, C. Vila, D. B. Stroppa, V. R. Mastelaro, J. Bettini, E. Longo and E. R. Leite, *J. Phys. Chem. C*, 2007, **111**, 5871–5875.

45 C. X. Kronawitter, J. R. Bakke, D. A. Wheeler, W. C. Wang, C. Chang, B. R. Antoun, J. Z. Zhang, J. Guo, S. F. Bent, S. S. Mao and L. Vayssières, *Nano Lett.*, 2011, **11**, 3855–3861.

46 J. Wan, W. Chen, C. Jia, L. Zheng, J. Dong, X. Zheng, Y. Wang, W. Yan, C. Chen, Q. Peng, D. Wang and Y. Li, *Adv. Mater.*, 2018, **30**, 1705369.

47 L. Li, J. Yan, T. Wang, Z. J. Zhao, J. Zhang, J. Gong and N. Guan, *Nat. Commun.*, 2015, **6**, 5881.

48 G. C. Vásquez, S. Z. Karazhanov, D. Maestre, A. Cremades, J. Piqueras and S. E. Foss, *Phys. Rev. B*, 2016, **94**, 235209.

49 S. O. Kucheyev, T. van Buuren, T. F. Baumann, J. H. Satcher, T. M. Willey, R. W. Meulenbergh, T. E. Felter, J. F. Poco, S. A. Gammon and L. J. Terminello, *Phys. Rev. B: Condens. Matter Mater. Phys.*, 2004, **69**, 245102.

50 W. Hu, L. Li, G. Li, Y. Liu and R. L. Withers, *Sci. Rep.*, 2014, **4**, 6582.

51 W. Hu, L. Li, W. Tong and G. Li, *Chem. Commun.*, 2010, **46**, 3113–3115.

52 H. Lin, L. Li, M. Zhao, X. Huang, X. Chen, G. Li and R. Yu, *J. Am. Chem. Soc.*, 2012, **134**, 8328–8331.

53 Y. Liu, J. Wei, Y. Tian and S. Yan, *J. Mater. Chem. A*, 2015, **3**, 19000–19010.

54 J. Ning, Q. Dai, T. Jiang, K. Men, D. Liu, N. Xiao, C. Li, D. Li, B. Liu, B. Zou, G. Zou and W. W. Yu, *Langmuir*, 2009, **25**, 1818–1821.

55 R. Kuriki, T. Ichibha, K. Hongo, D. Lu, R. Maezono, H. Kageyama, O. Ishitani, K. Oka and K. Maeda, *J. Am. Chem. Soc.*, 2018, **140**, 6648–6655.

56 T. Xia, N. Li, Y. Zhang, M. B. Kruger, J. Murowchick, A. Selloni and X. Chen, *ACS Appl. Mater. Interfaces*, 2013, **5**, 9883–9890.

57 L. Guan and X. Chen, *ACS Appl. Energy Mater.*, 2018, **1**, 4313–4320.

58 X. Chen, L. Liu, P. Y. Yu and S. S. Mao, *Science*, 2011, **331**, 746–750.

59 M. A. Green, J. Xu, H. Liu, J. Zhao, K. Li, L. Liu, H. Qin, Y. Zhu, D. Shen and X. Chen, *Mater. Today Phys.*, 2018, **4**, 64–69.

60 T. Xia, C. Zhang, N. A. Oyler and X. Chen, *Adv. Mater.*, 2013, **25**, 6905–6910.

